



ORIGINAL RESEARCH ARTICLE

Corrosion and Metallurgical Behavior of Wire Arc Additively Manufactured Functionally Graded Superduplex Stainless Steel/Inconel 625

Harshdeep Kaur, Siddharth Kumar, Dikshant Malhotra, and Tarun Nanda

Submitted: 15 June 2023 / Revised: 4 October 2023 / Accepted: 29 October 2023

Robotic cold metal transfer process was used for fabrication of wire arc additively manufactured (WAAM) wall involving a bimetallic combination of superduplex stainless steel (SDSS) and Inconel 625. A post-weld thermal aging treatment of 800 °C/2 h/water quenched was used to induce precipitation in the weld specimens. Aging resulted in the formation of intermetallics and carbides in the welds that caused their dendritic regions to be depleted in Cr, Ni and Fe, and enriched in C, as compared their respective matrix regions. X-ray photoelectron spectroscopy (XPS) studies on the passive layers show that the highest levels of Cr and Ni concentration were observed for SDSS and Inconel 625, respectively. Cyclic potentiodynamic polarization (CPP) testing results show that in the as-welded condition, bimetallic SDSS/In625 combination welds showed the highest pitting resistance followed by SDSS and Inconel 625. However, thermal aging degraded the pitting resistance of SDSS/In625 the most, followed by SDSS and Inconel 625. Tafel scan studies further show that in the as-welded condition, Inconel 625 exhibited better corrosion resistance than SDSS as well as SDSS/In625, but in the aged condition, bimetallic SDSS/In625 combination exhibited the highest corrosion resistance followed by SDSS and Inconel 625. This study shows that additive layers of Inconel 625 into WAAM fabricated SDSS structures can significantly improve their metallurgical and corrosion performance.

Keywords cold metal transfer, corrosion, Inconel 625, microstructure, superduplex stainless steel, wire arc additive manufacturing

1. Introduction

Engineering structures are designed and fabricated to serve efficiently without undergoing premature failures. Wire arc additive manufacturing (WAAM) is a process where arc energy is directed to produce parts/components without having to go for complicated set of tooling, molds or dies. Various materials that can be deposited through WAAM include C and low-alloy steels, different grades of stainless steels, Ni grades, Ti and various Al alloys as feed stock wire pertaining to each of these alloys is commercially manufactured and is readily available in the open market. One of the concerning points here is regarding the properties of the WAAM deposit. These properties are largely like welds, but in some cases significant differences are observed. The process variables as well as their precise control

are different from conventional robotic welding. Since this requires a deposition of multiple weld layers, it becomes important to get uniformly and consistently good weld bead geometry pertaining to each weld layer deposited. In general, dissimilar welding of Inconel alloys and SDSS has massive demand in high-temperature and high-corrosive-application industries. Advantages associated with functionally graded materials (FGM) are that they can provide different material properties in a single structure which are sometimes required to exhibit locally different material behaviors from parts used for various purposes in the industry. Currently much research has been focused largely on additive manufacturing (AM) and wire arc additive manufacturing (WAAM) in particular, which has emerged to be well suited for the design and fabrication of spatially dependent material combinations to achieve specific functions by grading chemical composition in a layer-by-layer manner. Functionally graded materials have proved their position among modern advanced materials.

Sasikumar et al. (Ref 1) highlighted the potential of WAAM to fabricate functionally graded material (FGM) with required properties with a viable manufacturing alternative to the traditional manufacturing techniques for producing FGMs. Srinivasan et al. (Ref 2) proposed a corrosion-resistant alloy of duplex stainless steel, functionally graded with carbon-manganese steel along with the inner layer for the risers to be used under the corrosive marine environment fabricated using cold metal transfer—gas metal arc welding, based on WAAM. The proposed FGM shows advantages in both strength and durability and hence is seen as a promising candidate for marine riser applications.

Harshdeep Kaur and Tarun Nanda, Mechanical Engineering Department, Thapar Institute of Engineering and Technology (TIET), Patiala 147004, India; Siddharth Kumar, Mechanical Engineering Department, Sant Longowal Institute of Engineering and Technology, Longowal, Punjab 148106, India; and Dikshant Malhotra, Department of Mechanical Engineering, Indian Institute of Technology Jammu, Jagti, Jammu and Kashmir 181221, India. Contact e-mail: harshdeepkaurs@yahoo.com.

Yusuf Ayan et al. (Ref 3) successfully fabricated low-alloy steel (ER70S-6) and austenitic stainless steel (308LSi) metal wires by the WAAM method and concluded that FGM structures with strong mechanical properties can be produced through WAAM. Rodrigues et al. (Ref 4) fabricated a functionally graded material (FGM) part by depositing a Cu-based alloy on top of a high-strength low-alloy (HSLA) steel by twin-wire and arc additive manufacturing (T-WAAM). It was reported that even though an abrupt transition was made with these two materials, the consequent remelting, and heating of previously deposited layers, when a new one is added, resulted in a large interface region (≈ 12 mm). This fact demonstrated the potential of WAAM to be used for FGM's fabrication. Yinbao Tian et al. (Ref 5) fabricated Ti-6Al-4 V and AlSi5 FGM and found that the interface layer between the Ti and Al alloys included a continuous layer and a discontinuous layer. Element Si was rich in the continuous layer, and the hardness and modulus of the interface layer were between those of Al and Ti alloys. Vahid A. Hosseini et al. (Ref 6) produced a functionally graded microstructure by the arc heat treatment of grade 2507 (UNS S32750) superduplex stainless steel under steady-state conditions for 10 h. The functionally graded material showed a clear correlation between secondary phase fractions and local hardness with an increased hardness in locations corresponding to sigma, R-phase and Chi precipitation as well as to heat treatment temperatures of 450-480 °C, correlating with the well-known 475 °C embrittlement, being related to the decomposition of ferrite which also produced a different etching response. Johnatan Rodriguez et al. (Ref 7) studied the fabrication of functionally graded structures of SS316L to Ni-based alloys using the novel technique 3D plasma metal deposition. Two Ni-based alloys were used: a heat resistance alloy Ni80-20 and the solid-solution strengthened Ni625. The as-built Ni625 microstructure was composed of an austenite (γ) matrix with secondary phases laves and δ -Ni3Nb, and precipitates M_7C_3 . The mixed zone exhibited the same phases but with changes in the morphology. Senthil et al. (Ref 8) used the cold metal transfer-based WAAM process to fabricate functionally graded Inconel 825-SS316L walls and concluded that both the Inconel 825 and SS316L sides had good fracture toughness.

Kumar et al. (Ref 9) have presented a comprehensive review of FGM literature, detailing the evolution and development history, classification and manufacturing methods for different types of FGMs, citing the merits and limitations of each. It is reported that owing to its graded function and agglomeration of contradictory properties over its structure, functionally graded materials (FGMs) are intended to optimize performance capability and survive in a harsh working environment without failure or losing their properties.

Lervåg et al. (Ref 10) fabricated WAAM wall of superduplex stainless steel (SDSS) using a wide range of heat inputs from 0.40 to 0.87 kJ/mm and reported that no intermetallic precipitation was observed in these walls. Sales et al. (Ref 11) reported on the outcomes of fatigue tests and fracture surface fractography of WAAM-processed SDSS. The results obtained indicated a significant anisotropy of fatigue properties and fatigue crack initiations resulting from internal defects rather than surface flaws. Di Zhang et al. (Ref 12) gave an overview of the up-to-date research status and future perspectives on the

additive manufacturing (AM) of duplex stainless steel (DSS) which is presented from extensive viewpoints including materials, processing, microstructure and properties. Kannan et al. (Ref 13) fabricated thin wall using ER2594 filler wire with the WAAM technology. It was reported that the austenite-ferrite fraction varied across the wall due to the complex cyclic thermal history during deposition. Detrimental phases such as sigma- σ or lambda- λ were not observed due to lower heat input and suitable interpass temperature. Yangfan et al. (Ref 14) demonstrated that the Inconel 625 alloys can be fabricated by cold metal transfer (CMT) process.

Few works are reported on using CMT-based WAAM for Ti-6Al-4 V and AlSi5 dissimilar alloys (Ref 15), effect of cooling rate and CMT mode process (Ref 16), effect of correction parameters on deposition characteristics (Ref 17), advanced CMT variants for steel-Al joints (Ref 18), heat accumulation effects on multilayer deposits of 316L (Ref 19), besides works on internal defects laser sensor monitoring (Ref 20), metal transfer behavior of Ti-6Al-4 V alloy (Ref 21), characterization of robotized CMT-WAAM steel (Ref 22), texture studies of 2205 duplex stainless steel (Ref 23), multi-response optimization for 308L (Ref 24) and spatters in CMT plus pulse-based WAAM for high-nitrogen austenitic stainless steels (Ref 25). There are few works where Inconel 625 and 718 have been used for fabricating functionally graded materials (FGM). Some of these are based upon direct laser deposition (DLD) process for Inconel 625 and AISI 431 (Ref 26), laser direct metal deposition (LDMD) (Ref 27) and direct energy deposition (DED) (Ref 28) for 316L/Inconel 625, 316L deposited upon Inconel 625 using laser (Ref 29), laser-based direct energy deposition of steel/inconel (Ref 30), selective laser melting (SLM) for Inconel 718 (Ref 31). WAAM has been used for depositing 316L clad layers (Ref 32) and fabricating FGM of SS321/Inconel 625 (Ref 33).

Literature review suggests that although a few studies related to the fabrication of superduplex stainless steel (SDSS) welds using wire arc additive manufacturing (WAAM) have been reported in the literature, scanty information is available on the functionally graded bimetallic materials involving SDSS and nickel superalloys using CMT-based WAAM technique in view of improving corrosion performance of SDSS structures.

FGMs similar to those studied in the present work have been fabricated (Ref 27-31), but not using the WAAM technique. These other studies in other AM processes such as laser bed fusion highlighted issues encountered that included segregation due to limited diffusion (Ref 27, 28), formation of detrimental phases (Ref 29), instability of molten pool (Ref 30) and porosity in selective laser melting (Ref 31). So based upon the literature review, it was observed that WAAM technique could be used to fabricate combination of materials like superduplex stainless steel and Inconel 625 and investigate it for its metallurgical and corrosion properties. Thus, the database generated based on such a material combination is expected to offer an engineering solution that would address issues of reinforcing/enhancing/modifying the properties of superduplex stainless steel to prevent premature failures and hence improving service performance and reliability of structures exposed to challenging corrosive environments, especially in sectors like renewable energy and oil and gas exploration.

2. Materials and Methods

The base plate/substrate comprised of rolled duplex stainless steel standard grade DSS 2205 and the solid filler wires of SDSS and standard grade of Inconel 625, of 1.2 mm diameter each, and the chemical composition of both wires is mentioned in Table 1.

Robotic-based CMT process was used to fabricate the WAAM wall which comprised largely of weld layers of SDSS to which three layers of Inconel 625 were added. The welding conditions used for fabrication of this wall are presented in Table 2, and these conditions were selected considering smooth, stable and spatter-free operation associated with the welding process.

Figure 1(a) shows the WAAM wall after machining out from the substrate and Fig. 1(b) shows red hot condition on the topmost weld layer, which was carefully observed, and the next weld layer was laid down only when the previous layer was cooled down to below 150 °C which is referred to as interpass temperature. Interpass cleaning was not required as the process gave spatter-free and clean weld surface finish indicating the potential capability of this process in maintaining stable welding conditions. WAAM deposition strategy included laying a total of 20 layers for fabricating the WAAM wall comprising 17 layers of SDSS and 3 layers of Inconel 625.

Different weld specimens extracted from the wall were subjected to a post-weld thermal aging treatment of 800 °C/2 h followed by water quenching, to induce precipitation and study its consequential effects on metallurgical and corrosion behavior of this wall. Different weld specimens like sole SDSS and Inconel 625 as well as bimetallic combination of SDSS/In625 were extracted from this wall and were characterized using optical microscopy, FESEM microscopy with EDS and EPMA-WDS technique. Besides this EBSD studies were also performed on SDSS.

Microhardness values in HV were measured using loading conditions of 1000 g and a dwell time of 20 s. Microstructural features of weld specimens extracted from different locations in the as-welded as well as thermally aged condition of 800 °C/ 2 h (water quenched) were observed using inverted metallurgical optical microscope. Standard metallographic procedures were used for preparing different weld specimens for optical microscopy. These procedures included polishing of the surface of the weld specimens up to 3000 grit size followed by lapping using alumina powder and diamond polish of 3 micron size to achieve a mirror finished surface. Thereafter, these polished surfaces of SDSS weld specimens were etched using carpenters etchant consisting of ferric chloride (8.5 g), cupric chloride (2.4 g), hydrochloric acid (122 ml), ethanol (122 ml) and nitric acid (6 ml) using immersion method. Inconel 625 surfaces were etched with waterless Kalling's reagent (CuCl₂ + 100 ml HCL + 100 ml C₂H₅OH) using cotton swab method. Different weld specimens were characterized for their microstructures as well as EDS mappings using FESEM (model: JSM 7610F plus; make: Jeol, Japan) equipped with EDS (make: EDAX, USA).

The qualitative phase analysis of different weld layers was done by x-ray diffraction (XRD) (make: Bruker, model: D8 Advance) technique using Cu K_α radiation (wavelength, λ = 1.54060 Å). The XRD spectra were generated within an angular range of 30° to 100° (2θ). The current and voltage used for XRD analysis were 40 mA and 40 kV, respectively.

The segregation tendencies of vital elements such as Fe, Cr, Ni and C were examined through microcomposition analysis at

Table 1 Chemical composition of Inconel 625 (UNS N06625) and SDSS in weight %)

Elements	Cr	Fe	Mo	Nb + Ti	C	Mn	Si	P	S	Al	Ti	Co	Ni	N
Inconel 625	20-23	5 max.	2.3	3.15-4.15	0.1 max.	0.5 max.	0.5 max.	0.015 max.	0.015 max.	0.4 max.	0.4 max.	1 max.	58 min.	...
SDSS	29	Balance	2.3	...	≤ 0.03	1	0.3	≤ 0.03	≤ 0.03	6	0.35

Table 2 Welding conditions used in the present work

Process parameters	Value
Welding current	225 A
Voltage	19.4 V
Travel speed	25 cm/min
Wire feed speed	9.5 m/min
Shielding gas flow rate	Industrially pure argon 20L/min
Arc weave	1.5 mm
Starting current	135%
Interpass temperature	150 °C

various dendritic as well as matrix regions of SDSS, Inconel 625 and SDSS/In625 interfacial regions using electron probe microanalyzer (EPMA) attached with wavelength-dispersive spectrometers (WDS) (4 numbers). EPMA-WDS maps of the above-mentioned elements were performed with beam of spot size 1 μm , probe current 2.008×10^{-8} A and accelerating voltage of 25 kV. One of the samples of SDSS taken from the center of the WAAM wall was also characterized by EBSD after electropolishing its surface with a solution of 80 ml methanol and 20 ml perchloric acid.

For studying corrosion behavior of different welds, two electrochemical methods, viz. cyclic potentiodynamic polarization (CPP) (for determining susceptibility to pitting corrosion) and Tafel scan (for calculating general corrosion rates), were used. For CPP and Tafel scans, potentiostat (make: Gamry Instruments; model: Reference 600) was used and tests were conducted at room temperature (25 °C). Three electrode paracell (counter electrode: graphite, reference electrode: saturated calomel electrode (SCE) and working electrode: samples extracted from the fabricated wall) was used. The electrolytic solution used in the paracell was 3.5 wt.% NaCl, and before commencement of each test, each weld sample was immersed in the electrolytic solution in the paracell for 30-minute duration to attain stable open-circuit potential (OCP). The weld samples were polished (up to 2000 grit size), and 28.26 mm² area was exposed to the electrolytic solution.

The experimental procedure used for CPP test was as per ASTM G-61 standard. The potential scan comprised of initial anodic scan followed by reverse scan with a scan rate of 0.16666 mV/s. The forward anodic scan was done from – 100 mV vs. OCP and continued till either of apex potential of 1500 mV or apex current of 10 mA/cm² was reached. When the apex value was reached, reverse scan started and got traversed toward the starting point.

The Tafel scan consisted of cathodic and anodic polarization, and the tests were conducted from an initial potential of – 0.25 V vs. Eoc till the final potential of 0.25 V vs. Eoc. The scan rate used for Tafel scan of different weld samples was 0.125 mV/s.

The vital elements such as Cr, O and Ni chemical concentrations in the passive film formed on SDSS, Inconel 625 and interfacial region of SDSS/In625 were estimated thorough x-ray photoelectron spectroscopy (XPS). The chemical concentrations of these elements were evaluated across the passive film. The x-ray source was monochromatic (Al-K α , $h\nu = 1486.6$ eV) for determining the chemical concentration depth profiles of Cr, O

and Ni. Cr2p, Ni2p and O1s XPS regions were scanned for depth profiles and Ar⁺ ions' sputtering was done. Prior to XPS analysis, passive films were formed electrochemically on polished samples through anodic polarization scan using same potentiostat as used for CPP and Tafel scan studies. The electrochemical passive film was formed by anodic scan till ending potential, which was in the passive region near to the pitting potential. The samples with electrochemically formed passive film were then rinsed in distilled water and dried for XPS studies.

3. Results and Discussion

3.1 Microhardness of WAAM Layers

Microhardness measurements taken at different locations at the WAAM wall and covering all 20 layers are graphically shown in Fig. 2. Each value presented is the average of two values taken at similar locations adjoining to each other on the wall.

Microhardness values of superduplex stainless steel (SDSS) specimens in the as-welded condition ranged from 280.6 to 291.7 VHN for the 14 layers starting from the bottom to the top. For the 3 layers of Inconel 625, while traversing from top to the bottom of the wall microhardness ranged from 242.9 to 258.9 VHN (as-welded) and from 231.3 to 264.1 VHN (aged), respectively. These low values of microhardness of Inconel 625 as compared to SDSS could probably be attributed to the fact that Inconel 625, by virtue of its higher Ni content, is reported to be usually ductile and softer than SDSS. Further, the topmost 3 layers of SDSS showed microhardness ranging from 296.3 to 348 VHN (for both as-welded and aged conditions) which was relatively greater than their counterparts at the bottom region. Higher microhardness of the top SDSS layers could be attributed to relatively higher cooling rates that prevailed during welding while these layers were laid.

Under aged condition of 800 °C/2 h, followed by water quenching, the microhardness of first 14 layers of SDSS layers raised to higher values ranging from 373.4 to 446.4 VHN, whereas top 3 SDSS layers showed microhardness ranging from 314.8 to 444.8 VHN. This significant decrease in the microhardness of SDSS layers could probably be attributed to precipitation that occurred in the aged weld layers. Unlike SDSS, aged Inconel 625 layers experienced a decrease in the microhardness values and ranged from 231.3 to 251.4 VHN. The relatively small decline in the microhardness of Inconel 625 layers was attributable to its inherent thermal stability that was maintained even at high temperatures. Thus, it could be observed that post-weld thermal aging induced more microhardness variation in SDSS layers than Inconel 625 layers.

3.2 Microstructure of WAAM Layers

Weld specimens extracted from different regions/locations of the WAAM wall were studied to understand their microstructural features. Figure 3(a) and (b) shows various phases present in SDSS specimen in the bottom region and in the 4th layer from bottom in the as-welded condition, respectively. As can be seen that in the bottom most layer, firstly grain boundary austenite (GBA) solidifies from the

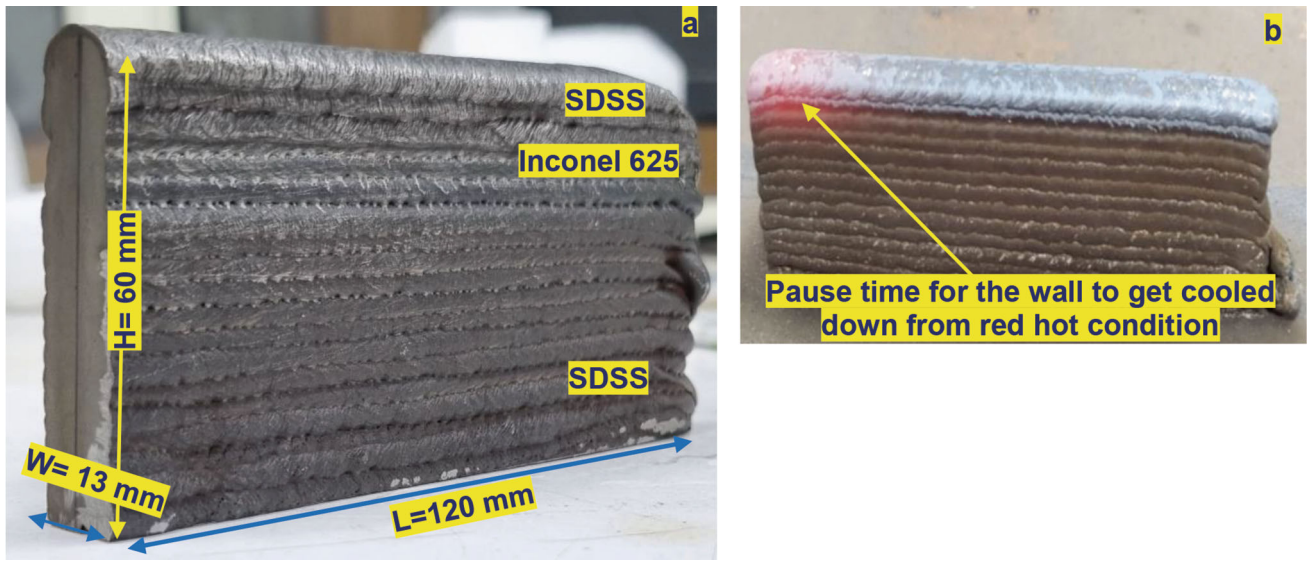


Fig. 1 (a) WAAM wall after removing/machining out the substrate plate; (b) maintaining interpass temperature

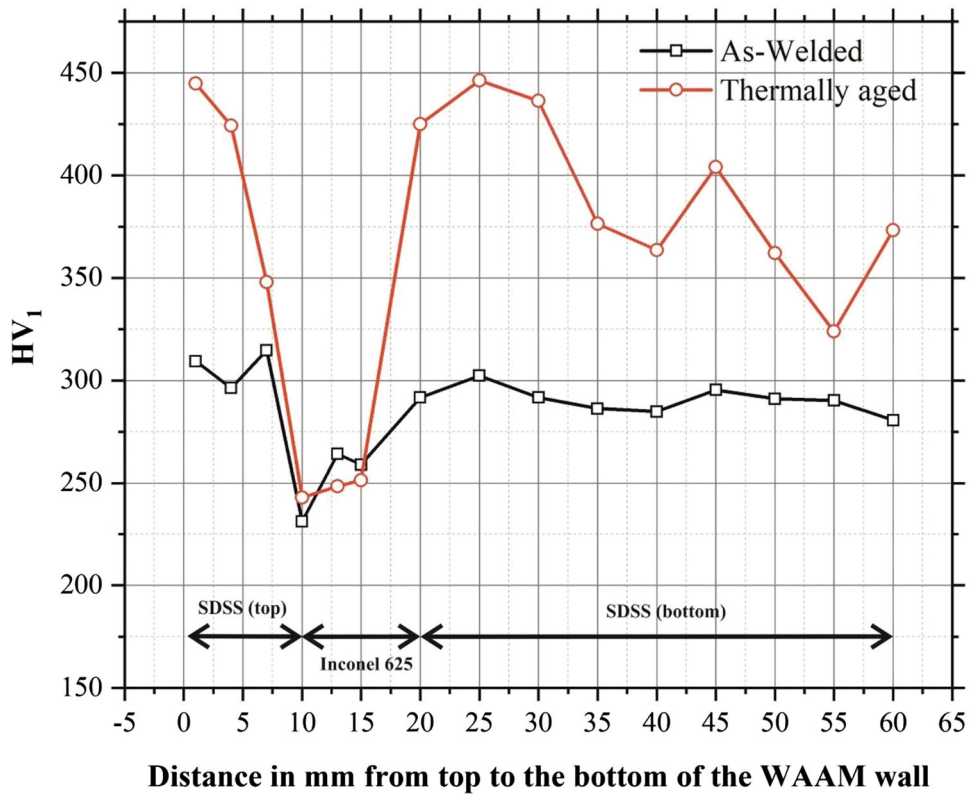


Fig. 2 Microhardness variation across different weld layers of WAAM wall measured from the top to the bottom of the wall

ferrite phase, and then, Widmanstätten austenite (WA) predominantly nucleates from GBA. At the same time, austenite nucleates intragranularly within the ferrite matrix depending upon the conditions that promote its formation and is referred to as intragranular austenite (IGA). Finally, upon completion of solidification the untransformed ferrite remains as ferrite.

However, in the 4th layer of SDSS, austenite appears as clustered IGA, elongated IGA, and thin and discontinuous WA which are attributable to relatively higher cooling rate experienced by this weld layer. The main reason that the bottom weld layer experienced slower cooling rate than its upper counterpart is that when welding was done, heat conducted through the

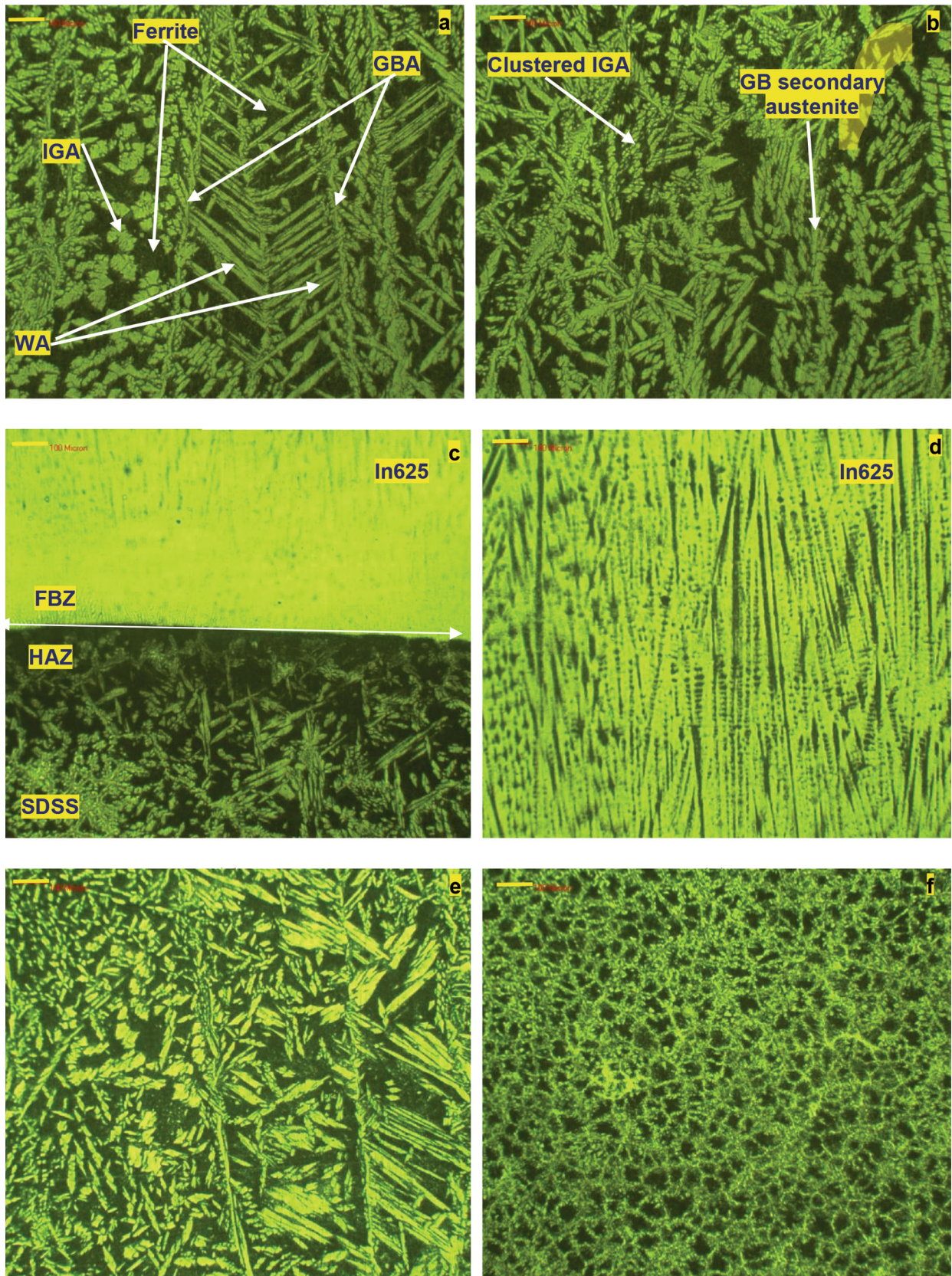


Fig. 3 (a) Photomicrograph of SDSS bottom layer (100X)—as-welded. (b) Photomicrograph of SDSS 4th layer from bottom (100X)—as-welded. (c) Photomicrograph of the composite zone SDSS/In625 (100X)—as-welded. (d) Photomicrograph showing upper region of In625 (100X)—as-welded. (e) Photomicrograph showing SDSS weld layer middle region (100X)—aged. (f) Photomicrograph showing SDSS top layer of the wall (100X)—aged

Table 3 EDS results showing chemical composition in different weld layers taken at different locations

Region of wall	Element, wt. %						
	Cr	Mn	Fe	Ni	Mo	Co	Nb
SDSS (bottom region)	31	1	59.9	6	1.9
SDSS (middle region)	29.7	...	61.7	6.3	1.3	0.7	0.2
Interfacial SDSS/In625 (lower region)	27.7	1.4	34.7	30.2	5.4	0.6	...
Inconel 625 (middle region)	25.3	...	8	58.1	5.8	...	2.8
	25.1	...	6	59.7	6.5	...	2.7
	24.4	...	4.3	62	6.2	...	3.1
Interfacial SDSS/In625 (upper region)	27.3	1	28.8	37.2	3.8	0.5	1.5
SDSS/In625 (top region)	30	...	50.3	16.5	2.5	...	0.7

base plate and after sometime this base plate picked up and accumulated heat such that overall heat dissipation via conduction became slower, thus resulting in relatively slower cooling rate. Differential cooling rates experienced by these weld layers are also evident from the microhardness of these layers as discussed previously.

Figure 3(c) shows the microstructure of the interfacial region of SDSS/In625 where fusion boundary zone (FBZ) and grain-coarsened heat-affected zone (HAZ) in the SDSS region were observed. Due to crystal structural differences, non-epitaxial growth was observed at the interface of this weld specimen. Figure 3(d) shows Inconel 625 microstructure where large grains containing columns of parallel microdendritic microstructure in the austenite matrix were observed. Figure 3(e) and (f) shows the aged SDSS weld specimen at the middle region and the top region of the wall. Figure 3(e) shows specifically that conventional morphology of GBA, WA and IGA was noticeably absent which was attributable to highest cooling rates experienced by the top region of the weld wall.

3.3 EDS Analysis of WAAM Layers

Table 3 presents results of the EDS studies performed selectively on SDSS, SDSS/In625 and Inconel 625 specimens taken from different locations of the WAAM wall. These results indicate the effect of mixing of SDSS with Inconel 625 and it is observed that there existed compositional gradients across the interfacial regions of this bimetallic combination. However, full filler chemistry was achieved by Inconel 625 in the middle location of the layers as dilution effects by SDSS here were insignificant. Another noticeable observation is that the composition of SDSS was altered at the interfacial regions and it became richer in Ni, Mo, Co and Nb due to mixing/fusing with Inconel 625. In general, diffusion of various vital elements was observed in both SDSS and Inconel 625, indicating good metallurgical compatibility of both alloys. EDS studies were further extended for studying the precipitation effects due to aging in different specimens in the aged condition. As shown in Fig. 4(a), two area spectra, viz. 1 and 2, and one spot spectrum were selected and their EDS compositions are presented adjacent to the SEM micrograph that was taken at 1000X magnification. A noticeable observation here is with regard to Spot 3 which shows that there was a significant rise of Mo and N accompanied by fall of Ni. Such a composition indicated the

probable formation of sigma phase as well as nitrides and their preferential occurrence in the interdendritic regions in SDSS.

3.4 XRD Analysis of WAAM Layers

Different samples were subjected to XRD evaluation, and the results are presented in Fig. 5.

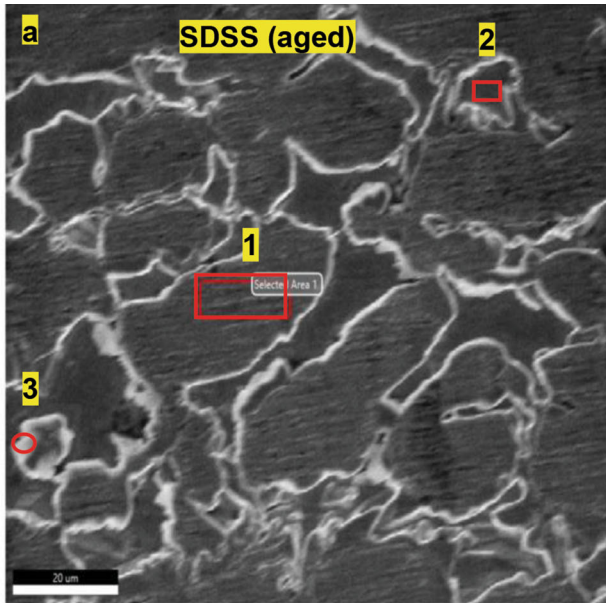
Different phases, intermetallics and carbides identified for different weld specimens are also presented in Table 4, and the information about their respective lattice, space group and PDF card numbers is summarized in Table 5.

From these studies, it is observed that besides retaining almost all the phases that were there in the as-welded condition as shown in Fig. 5(a); additionally, few more phases appeared in the welds aged at 800 °C/2 h as shown in Fig. 5(b). For instance, aged SDSS specimen had sigma phase formed in it, bimetallic combination SDSS/In625 in the aged condition indicated the formation of NbC, γ'' (Ni₃Nb) and Laves (Ni₂Ti and Cr₂Ti), and aged Inconel 625 contained Laves (Ni₂Ti) phase.

3.5 EBSD Characterization of SDSS Weld Layers

Figure 6 presents the results of the EBSD studies performed on SDSS specimen. Grain orientation is revealed by a color-coded figure called as inverse pole figure (IPF) map which is shown in Fig. 6(a).

The area of IPF map with identical color specifies identical orientation of austenite as well as ferrite. Inverse pole figures as in Fig. 6(a) show that extent of degree of randomness of grains in austenite was more than in alpha ferrite. Further grains of IGA were more randomly oriented than those of GBA and WA. As shown in Fig. 6(b) which is the misorientation angle chart, fraction of low-angle grain boundary (LAGB) taken as 2° to 10° was relatively less than high-angle grain boundary (HAGB) taken as greater than 10° (Ref 33). Further, number fraction of more than 0.1 pertains to the grains with boundary angles of 44.05° and 58.55° and there was a negligible fraction of grains with grain boundaries having angles lying in the range of 9.25° to 32.45°. Local strain distribution in microstructure is calculated by Kernel average misorientation (KAM). Figure 6(c) shows a color variation in KAM map which indicates non-homogeneous distribution of local strain across the microstructure. Thick block morphology of Widmanstätten austenite



Wt. %	Cr	Fe	Ni	Mo	N
1	20.8	66.4	5.8	1.5	-
2	28.1	66.1	4.8	0.7	0.4
3	24.0	59.5	2.4	8.5	5.7

1: Area spectrum taken at large grained matrix region.

2: Area spectrum small grained matrix region.

3: Spot spectrum taken at grain boundary region

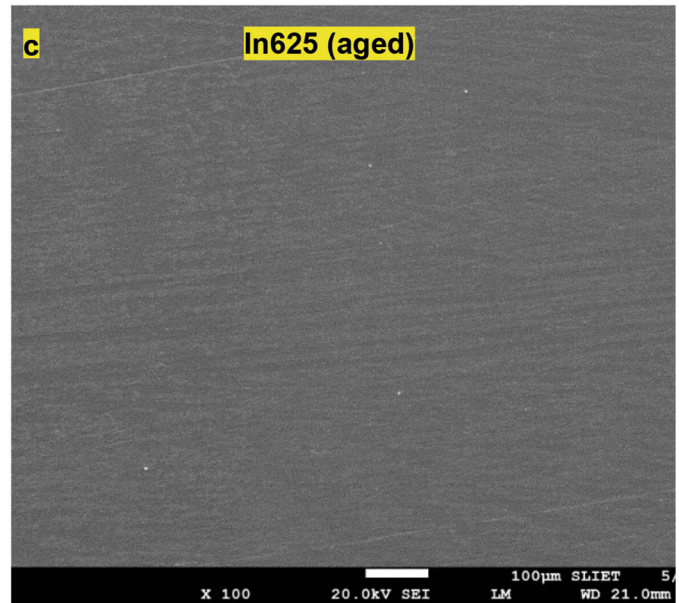
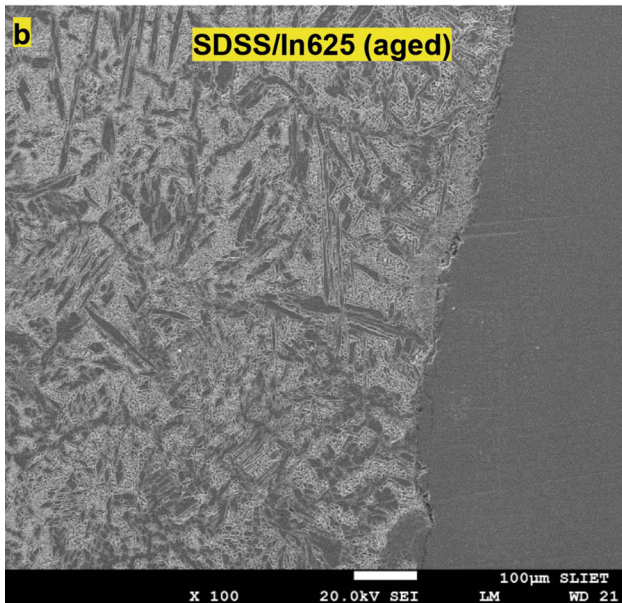


Fig. 4 (a) FESEM micrographs of aged, (a) SDSS, (b) interfacial regions of SDSS/In625, (c) Inconel 625 taken, on the WAAM wall at different locations

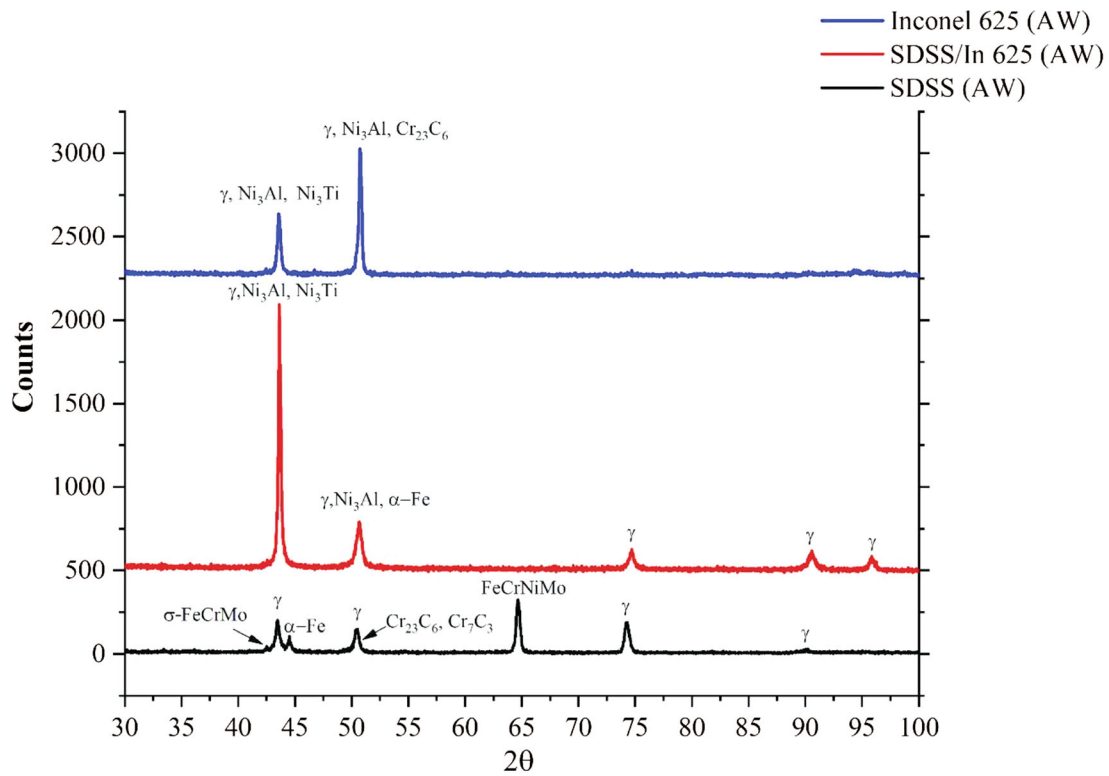
(WA) showed relatively uniform distribution of local strain than the grain boundary austenite (GBA) that had intragranular austenite (IGA) on the one side and thin parallel WA distributed skeletally on the other side. A large fraction of lower KAM values as observed in Fig. 6(d) was due to a greater degree of randomness of the grains. Figure 6(e) which is a color-coded phase map shows that fraction of austenite and ferrite was 0.657 and 0.343, respectively.

3.6 EPMA Studies of WAAM Layers

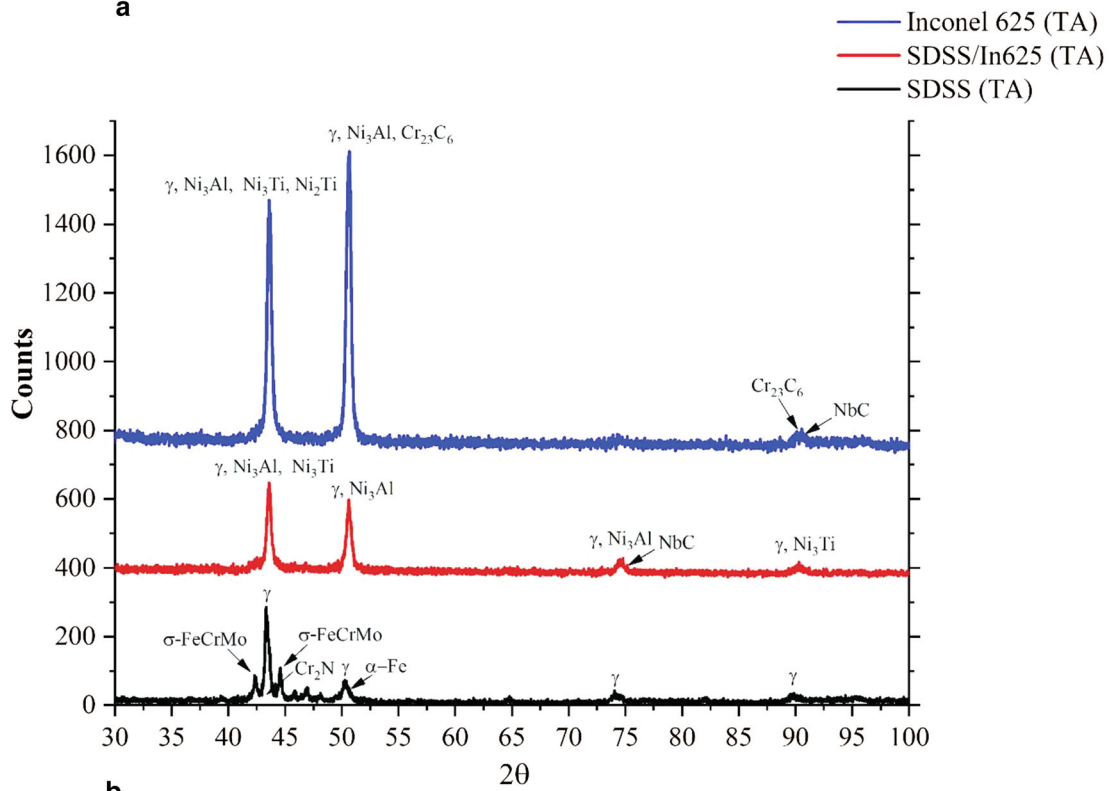
EPMA-WDS spot and mapping results at the interfacial region of Inconel 625 and SDSS are shown in Fig. 7 (as-welded

condition) and Fig. 8 (aged condition). The spot locations were taken at SDSS/In 625 interfacial region, dendrite and matrix regions of both SDSS and Inconel 625. The chemical composition of Cr, Ni, Fe and C at each of the mentioned locations are listed in Table 6.

For SDSS and Inconel 625, dendrite regions were observed to be depleted in Cr, Ni and Fe, and enriched in C relative to their respective matrix. Under the aged condition, the trend of rise and fall of these elements was the same with the only difference that the rise of C was relatively high as compared to the as-welded condition. Such a rise of C indicated that presence of carbides occurred interdendritically, thus making SDSS susceptible to corrosion.



a



b

Fig. 5 XRD spectra for different weld specimens (a) in the as-welded condition, (b) aged condition

Table 4 XRD analysis of different weld samples

Condition	Sample	Phases identified
As-welded	SDSS (AW)	Austenite, α -ferrite, Cr ₂₃ C ₆ , Cr ₇ C ₃
	SDSS/Inconel 625 (AW)	Austenite, Cr ₂₃ C ₆ , intermetallic γ' (Ni ₃ Al-fcc and Ni ₃ Ti-hexagonal)
	Inconel 625(AW)	Austenite, α -ferrite, Cr ₂₃ C ₆ , intermetallic γ' (Ni ₃ Al-fcc and Ni ₃ Ti-hexagonal), Laves (Ni ₂ Ti)-hexagonal
Aged at 800 °C/2 h/ water quenched	SDSS (TA)	Austenite, α -ferrite, σ -Fe, Cr ₂ N
	SDSS/Inconel 625 (TA)	NbC, Cr ₂₃ C ₆ , intermetallic γ' (Ni ₃ Al-fcc and Ni ₃ Ti-hexagonal), γ'' (Ni ₃ Nb)-bcc, Laves (Ni ₂ Ti and Cr ₂ Ti)-hexagonal and austenite
	Inconel 625 (TA)	Cr ₂₃ C ₆ , intermetallic γ' (Ni ₃ Al-fcc and Ni ₃ Ti-hexagonal), Laves (Ni ₂ Ti)-hexagonal and austenite

Table 5 Lattice, space groups and PDF card numbers of different phases identified through XRD evaluation of weld layers

Phase	Lattice	Space group	PDF card number
Austenite (γ)	Cubic	Fm-3 m (225)	PDF 00-023-0298
α -Ferrite	Orthorhombic	Pnma (62)	PDF 00-003-0411
Cr ₂₃ C ₆	Orthorhombic	Fm-3 m (225)	PDF 00-003-1172
Cr ₇ C ₃	Orthorhombic	Fm-3 m (225)	PDF 00-006-0683
Ni ₃ Al	Cubic	Pm-3 m (221)	PDF 00-009-0097
Ni ₃ Ti	Hexagonal	Fm-3 m (225)	PDF 00-002-1234
Ni ₂ Ti	Rhombus H. axes	R-3 m (166)	PDF 01-072-2619
σ -FeCrMo	Tetragonal	P42/mnm	PDF 00-009-0050
NbC	Cubic	Fm-3 m (225)	PDF 00-002-1031
Cr ₂ Ti	Cubic	Fd-3 m (227)	PDF 00-005-0713

3.7 Corrosion Behavior of WAAM Layers

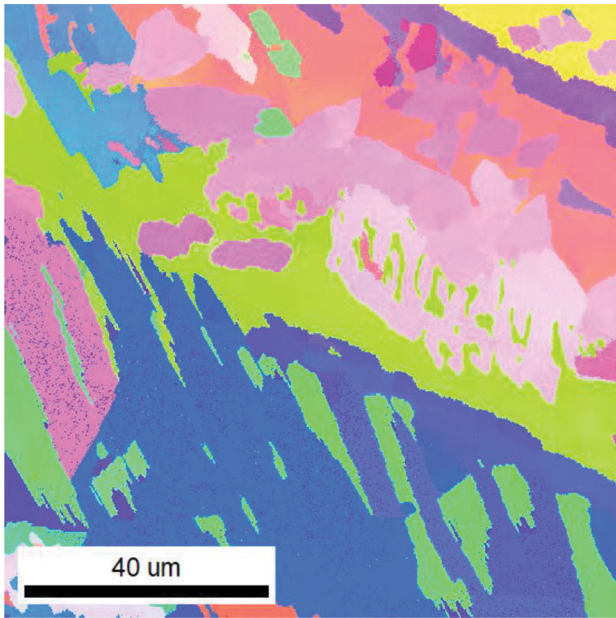
Weld specimens extracted from different regions/locations of the WAAM wall were evaluated for studying their corrosion behavior, both localized and general corrosion, and the same are discussed as follows:

3.7.1 Cyclic Potentiodynamic Polarization (CPP) testing results of WAAM layers. CPP curves obtained after testing of different weld specimens are shown in Fig. 9(a) for SDSS (as-welded and thermally aged), Fig. 9(b) for Inconel 625 (as-welded and thermally aged) and Fig. 9(c) for composite region SDSS/In625 (as-welded and thermally aged). The results extracted from these CPP curves are presented in Table 7. Cyclic potentiodynamic polarization (CPP) testing was performed twice on each specimen but on a new location with a fresh surface, and the results reported in Table 7 are the average of the two readings.

As seen from the CPP results in Table 7, it is observed that unaged SDSS/In625 weld specimen showed the highest pitting potential of 840.8 mV indicating its highest pitting resistance among all other specimens in the as-welded condition. However, when aged it showed a drastic reduction in its pitting resistance as its pitting potential falls to 372.1 mV. This loss of pitting resistance was attributable to the formation of NbC and γ'' (Ni₃Nb) in the interfacial region of SDSS/In625.

Further, SDSS specimen showed the pitting potential of 737.7 mV, but no passivation characteristics were observed, and it reduced to 466.9 mV when aged. This loss of pitting resistance was attributable to the formation of sigma phase and chromium nitride that played a detrimental role in decreasing the pitting resistance of SDSS. A similar role of sigma phase formation in SDSS (Ref 35-37) as well as SDSS welds (Ref 34) aged in the range of 750-850 °C has been reported to be detrimental for their pitting performance. Inconel 625 specimen showed good pitting resistance with pitting potential of 623.7 mV with less degradation down to 476.7 mV when aged, and exhibited good re-passivation characteristics. Relatively lesser degree of pitting resistance degradation was attributable to the absence of detrimental phases in Inconel 625 in the aged condition.

Further, while comparing the pitting performance based on values of corrosion potential (E_{corr}), as measured in the present case, it is observed that in the as-welded condition, E_{corr} of SDSS > Inconel 625 > SDSS/In625 which was attributable to a decrease in the anodic reaction with the growth of a passive film or increase in the cathodic reaction. Thus, the pitting resistance degradation of various weld specimens due to aging and based upon measured E_{pit} values, the trend observed was that SDSS showed a loss of 36.7 %, SDSS/In625 a loss of 55.74 % and

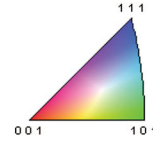


a

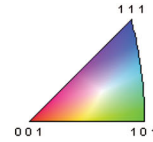
Color Coded Map Type: Inverse Pole Figure [001]

Crystal direction

Fe (gamma, austenite, fcc)



Fe (alpha, ferrite, bcc)



Fe Cr Mo (sigma)

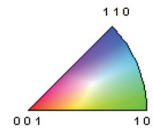


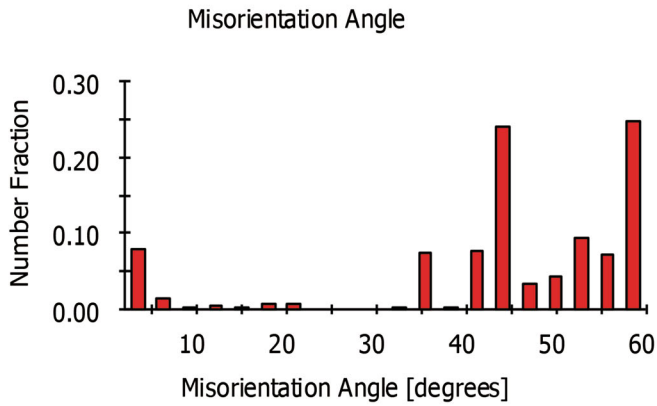
Chart: Misorientation Angle

Angle [degrees]	Number Fraction
3.45	0.0780946
6.35	0.0133263
9.25	0.00289614
12.15	0.00516445
15.05	0.0016911
17.95	0.00759478
20.85	0.00799984
23.75	0.000658214
26.65	1.01264e-05
29.55	0.000526572
32.45	0.00208603
35.35	0.0740036
38.25	0.00183287
41.15	0.0769605
44.05	0.239631
46.95	0.0326677
49.85	0.0429561
52.75	0.0926361
55.65	0.0728593
58.55	0.246405

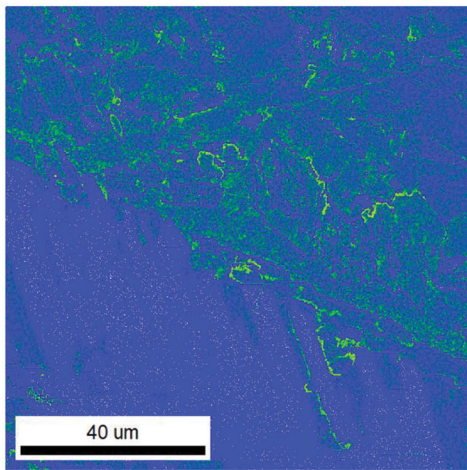
Summary Statistics [degrees]

Average:

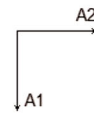
Number 44.353



b



c



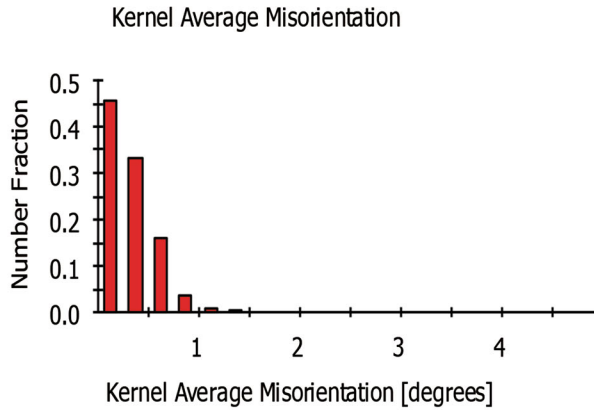
Gray Scale Map Type: <none>

Color Coded Map Type: Kernel Average Misorientation

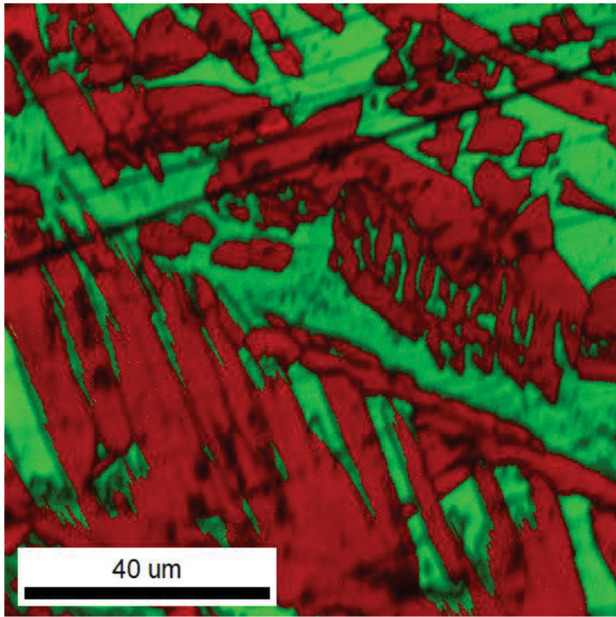
Min	Max	Total Fraction	Partition Fraction
0	4.95677	0.990	0.990

Boundaries: <none>

Fig. 6 (a) EBSD color-coded maps and pole figures of SDSS (as-welded) sample. (b) Misorientation angle chart. (c) Color-coded KAM map. (d) KAM misorientation chart. (e) Color-coded phase map



d



e

Chart: Kernel Average Misorientation

Avg Angle [degrees]	Number Fraction
0.123919	0.455678
0.371758	0.331419
0.619597	0.158864
0.867435	0.0361912
1.11527	0.00947317
1.36311	0.00357824
1.61095	0.00165479
1.85879	0.00102597
2.10663	0.00068917
2.35447	0.000471128
2.60231	0.000338745
2.85014	0.000208309
3.09798	0.000130436
3.34582	0.000105128
3.59366	6.03511e-05
3.8415	6.22979e-05
4.08934	1.36277e-05
4.33718	1.94681e-05
4.58502	1.16809e-05
4.83285	5.84043e-06

Summary Statistics [degrees]

Average:	
Number	0.290326
Standard Deviation:	
Number	0.298267



(Highlighted Points)/(Total Number of Points) = 0.000
 (Highlighted Points)/(Number of Good Points) = 0.000
 (Highlighted Points)/(Number of Partition Points) = 0.000

Gray Scale Map Type: Image Quality
 10775.4...52281.5 (10775.4...52281.5)

Color Coded Map Type: Phase

Phase	Total Fraction	Partition Fraction
Fe (gamma, austenite, fcc)	0.657	0.657
Fe (alpha, ferrite, bcc)	0.343	0.343
Fe Cr Mo (sigma)	0.000	0.000

Boundaries: <none>

Fig. 6 continued

Inconel a loss of 23.56 % as compared to their pitting resistance in the as-welded conditions, respectively.

3.7.2 Tafel Scan Results Testing Results of Welds. Tafel scan results after testing of different weld specimens are shown in Fig. 9(d) for SDSS (as-welded and thermally aged), Fig. 9(e) for Inconel 625 (as-welded and thermally aged) and Fig. 9(f) for composite region SDSS/In625 (as-welded and thermally aged). For calculating corrosion rate of weld surfaces, the

following formula was used:

Corrosion rate (mpy) = $0.13 \times i_{\text{corr}} \times E_w/d$, where I_{corr} is corrosion current, E_w is equivalent weight and d is density. The results extracted from these scans are presented in Table 8.

As can be seen from these results, in the as-welded condition, Inconel 625 showed least corrosion rate of $7.45\text{E}-08$ mpy followed by SDSS with $1.03\text{E}-07$ mpy and then SDSS/In625 with the highest value of $1.13\text{E}-07$. However, this trend changed

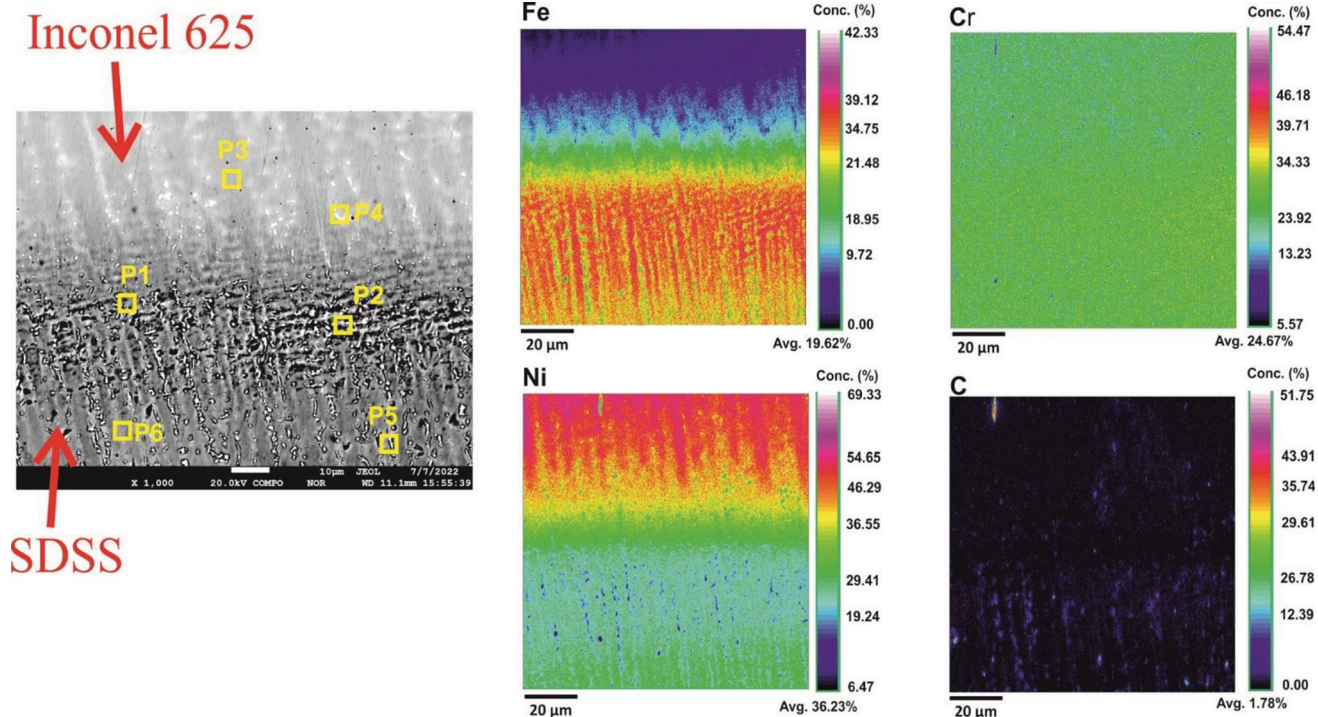


Fig. 7 SEM micrographs showing spot locations and EPMA-WDS mapping of Fe, Cr, Ni and C at the interfacial region of Inconel 625/SDSS in the as-welded condition

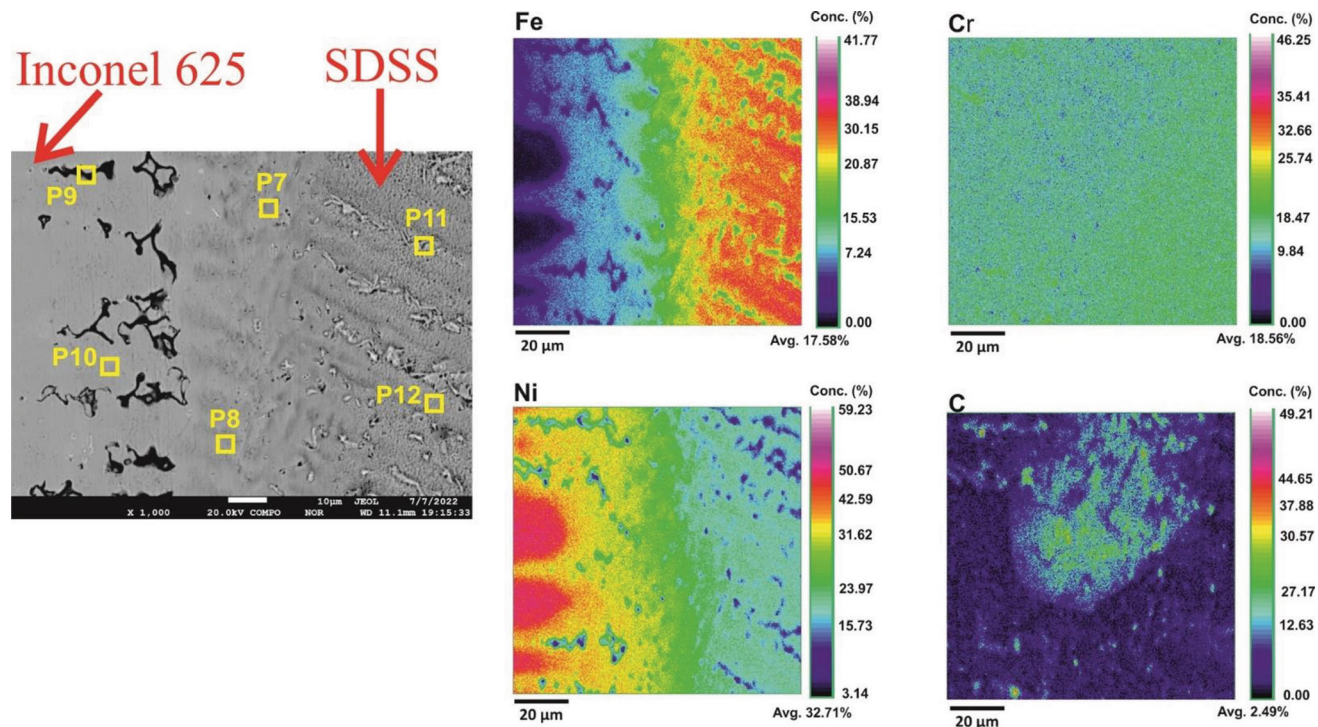


Fig. 8 SEM micrographs showing spot locations and EPMA-WDS mapping of Fe, Cr, Ni and C at the interfacial region of Inconel 625/SDSS at aged 800 °C/2 h condition

Table 6 EPMA-WDS spot locations for microcomposition analysis in wt.% of Fe, Cr, Ni and C at different locations in the interfacial region of Inconel 625 and SDSS

Type of weld	Regions	Fe	Cr	Ni	C
In625/SDSS (as-welded)	In625/SDSS (P1)	18.47	22.85	41.84	0.74
	In625/SDSS (P2)	30.12	25.69	33.27	0.25
	Inconel 625 Matrix (P3)	7.33	23.18	55.44	0.63
	Inconel 625 Dendrite (P4)	5.47	20.35	44.75	1.85
	SDSS Dendrite (P5)	37.48	25.87	5.15	1.35
	SDSS Matrix (P6)	49.76	29.35	8.54	0.19
In625/SDSS (Thermally aged)	In625/SDSS (P7)	28.19	24.86	23.66	0.36
	In625/SDSS (P8)	14.55	19.52	32.78	0.95
	Inconel 625 Dendrite (P9)	4.91	18.57	42.96	2.35
	Inconel 625 Matrix (P10)	8.56	22.79	54.43	0.71
	SDSS Dendrite (P11)	32.53	21.73	4.26	1.52
	SDSS Matrix (P12)	46.42	28.65	7.39	0.22

when welds were thermally aged at 850 °C/2 h (water quenched) and it was observed that specimen SDSS/In625 showed the least corrosion rate of 1.84E-7 followed by SDSS with 3.18E-1 mpy and then Inconel 625 with corrosion rate of 3.66E-1 mpy. Further it is observed that in the as-welded condition, when compared with SDSS, the corrosion rate was 9.70% higher in SDSS/In625 and 27.66% lower in case of Inconel 625.

3.7.3 XPS Analysis of WAAM Layers. The CPP results were further corroborated with XPS analysis of SDSS/In625 interfacial region, SDSS, Inconel 625 samples in the as-welded condition. Figure 10 presents different XPS depth profile concentrations for vital elements, viz. O, Cr and Ni. It is seen from this figure that the O concentration of all the samples gradually decreased across the passive film, while Cr and Ni concentration gradually increased. The passive film depth as measured at half the concentration of O concentration profile was estimated to be 4.56 nm for SDSS/In625(AW) interfacial region, 5.12 nm for SDSS(AW) and 5.33 nm for Inconel 625. At surface (0 nm), Cr concentration was observed to be highest for SDSS(AW) while Ni concentration was highest for Inconel 625 (AW) among all the samples. For the weld sample SDSS/In625(AW), the Cr and Ni concentrations were between both SDSS(AW) and Inconel 625. Previous reports suggest that higher concentrations of Cr and Ni tend to form a compact and dense passive film owing to the presence of greater concentrations of Cr and Ni oxides (Ref 38, 39).

4. Conclusions

Based upon the functionally graded WAAM wall of SDSS/Inconel 625 fabricated using robotic-based CMT process, the following conclusions are drawn:

1. SDSS wall with additive layers of Inconel 625 (bimetallic combination) fabricated using robotic-based CMT process was geometrically consistent with minimal distortion.
2. Lower portions of SDSS/In625 wall possessed relatively lower microhardness as compared to the upper ones indicating slower cooling rates experienced by the lower layers. Inconel 625 possessed lower microhardness than SDSS layers and thermal aging at 800 °C/2 h increased microhardness of both SDSS and Inconel 625 layers.
3. EPMA-WDS studies showed that for SDSS and Inconel 625, dendrite regions were depleted in Cr, Ni and Fe, and enriched in C relative to their respective matrix. The extent of depletion Cr, Ni and Fe and rise of C was relatively more in the aged welds.
4. CPP studies indicate that among all the specimens, SDSS/In625 unaged specimen showed highest pitting potential indicating highest pitting resistance. However, when aged it showed a drastic reduction in its pitting resistance.
5. XPS studies show that the O concentration of all the samples gradually decreased across the passive film, while Cr and Ni concentration gradually increased. At the surface, Cr concentration was observed to be the highest for SDSS while Ni concentration was highest for Inconel 625.
6. In the as-welded condition, the order of corrosion performance in the descending order was In625 > SDSS/In625 > SDSS. However, aging resulted in pitting resistance degradation for which SDSS showed a loss of 36.7%, SDSS/In625 a loss of 55.74% and Inconel 625 a loss of 23.56% when compared against unaged SDSS. Metallurgical and corrosion performance of SDSS can be enhanced by Inconel 625 additions made through WAAM

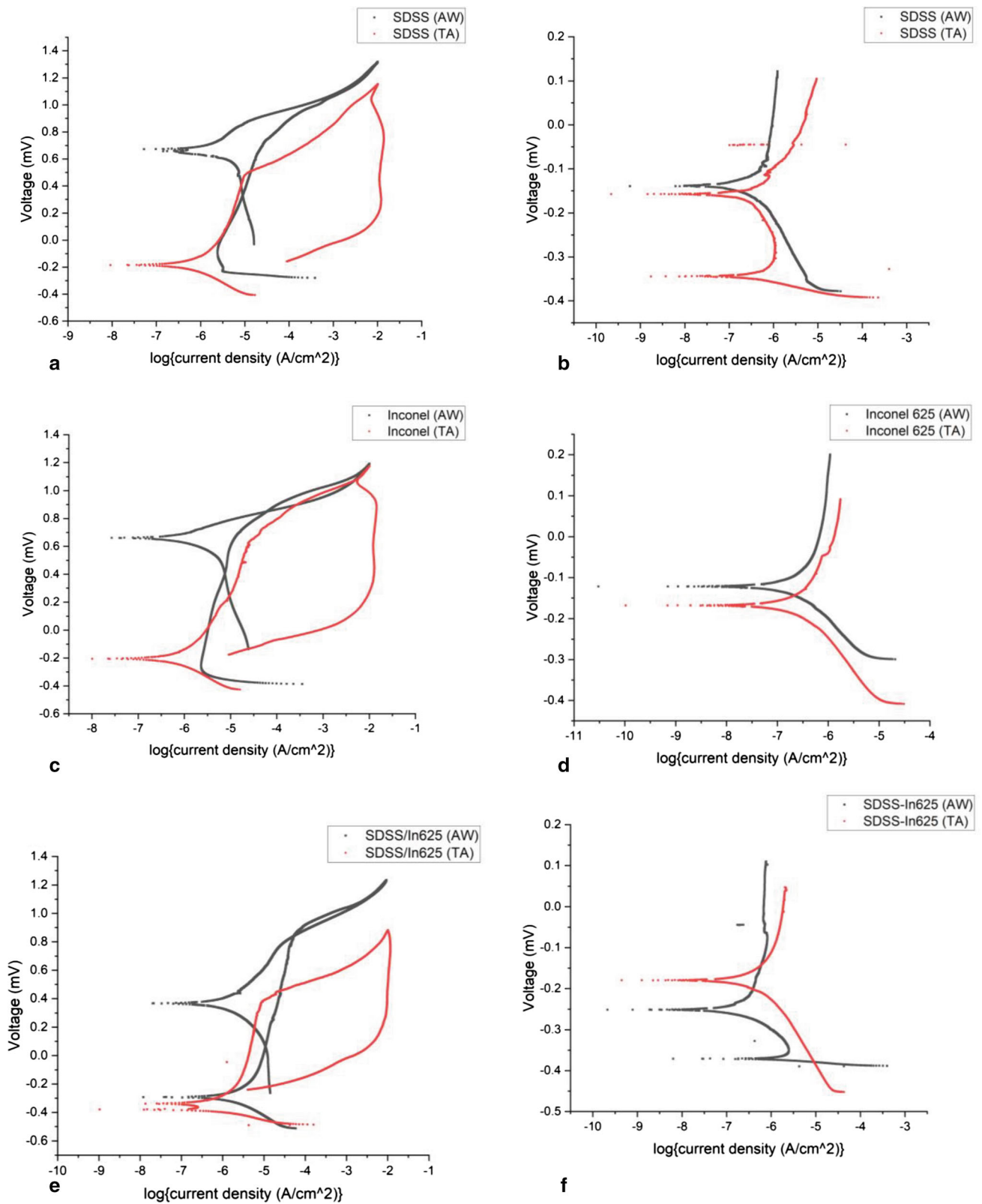


Fig. 9 CPP curves for (a) SDSS, (b) Inconel 625, (c) SDSS/In625; Tafel scan curves for (d) SDSS, (e) Inconel 625, (f) SDSS/In625 (AW: as-welded; TA: thermally aged at 850 °C/2 h)

Table 7 CPP testing results for different welds layers

Specimen condition	Corrosion potential (E_{corr})		Pitting potential (E_{pit})	
	As-welded, mV	Thermally aged, mV	As-welded, mV	Thermally aged, mV
SDSS	650	- 175	737.7	466.9
SDSS/In625	- 293.1	- 339.3	840.8	372.1
In625	661.5	- 205.7	623.7	476.7

Table 8 Tafel scan results for different weld layers

Values	I_{corr} A/cm ²		E_{corr} mV		Corrosion rate, mpy	
	As-welded	Thermally aged	As-welded	Thermally aged	As-welded	Thermally aged
SDSS	2.24E-7	6.97E-7	- 139.8	- 158	1.03E-07	3.18E-1
SDSS/In625	2.44E-7	3.98E-7	- 251.1	- 179.9	1.13E-07	1.84E-7
Inconel 625	1.61E-7	8.01E-7	- 122	- 168	7.45E-08	3.66E-1

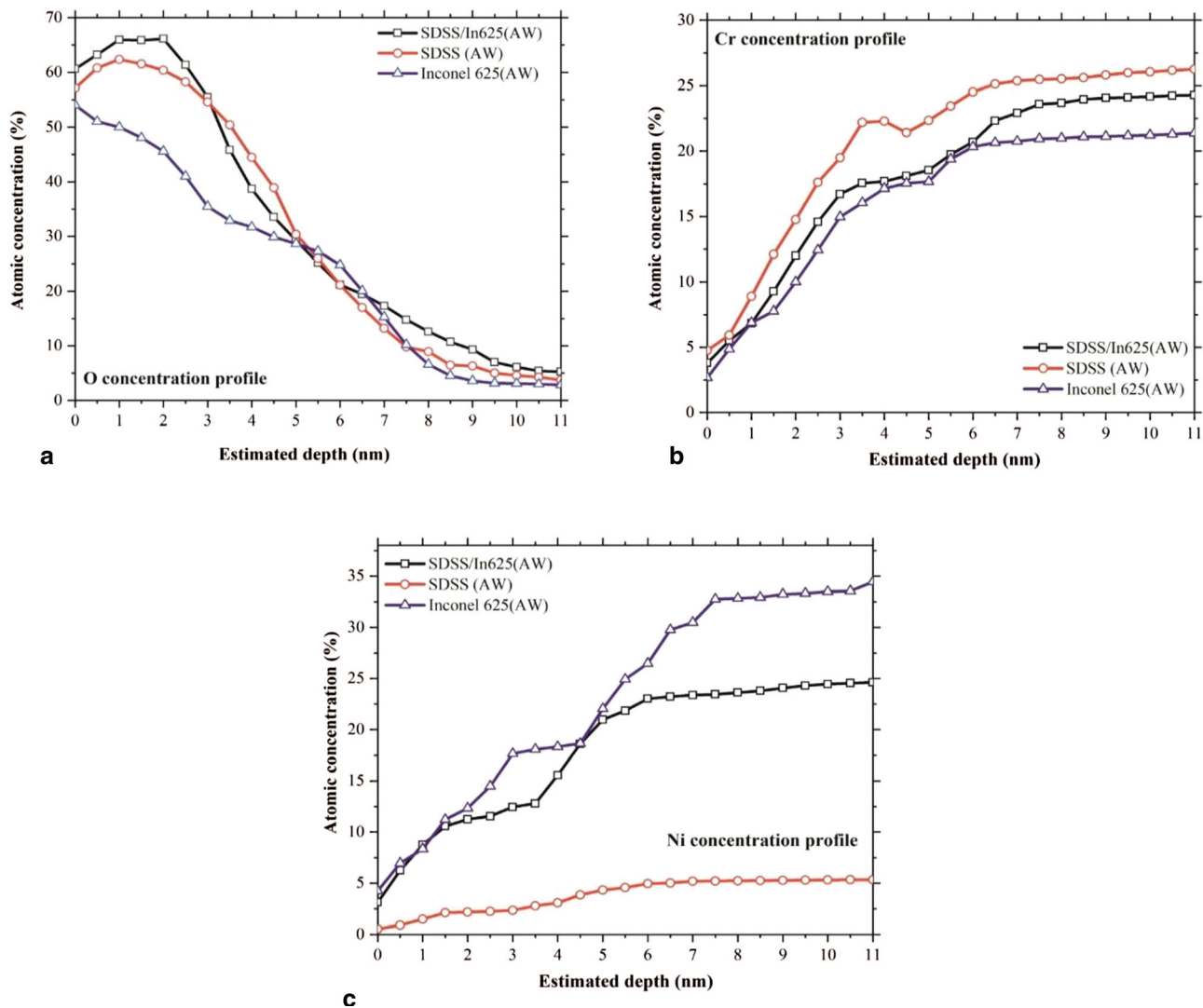


Fig. 10 XPS depth profile concentrations for vital elements for SDSS/In625, SDSS and Inconel 625 in the as-welded condition: (a) O concentration profile; (b) Cr concentration profile; (c) Ni concentration profile

technique which gives a bimetallic material combination with improved corrosion performance.

Acknowledgments

Authors gratefully acknowledge the infrastructural support provided by Welding Metallurgy Laboratory, Mechanical Engineering Department and FESEM as well as XRD facility at Central facility of Sant Longowal Institute of Engineering and Technology (SLIET), Longowal. Technical support rendered by Mr. Varinder Singh for robotic welding is also thankfully acknowledged.

Conflict of interest

The authors declare that they have no known competing financial interests or personal relationships that could have appeared to influence the work reported in this paper.

References

1. R. Sasikumar, A.R. Kannan, S.M. Kumar, R. Pramod, N.P. Kumar, N.S. Shanmugam, Y. Palguna, and S. Sivankalai, Wire Arc Additive Manufacturing of Functionally Graded Material with SS 316L and IN625: Microstructural and Mechanical Perspectives, *CIRP J. Manuf. Sci. Technol.*, 2022, **38**, p 230–242. <https://doi.org/10.1016/j.cirpj.2022.05.005>
2. S. Chandrasekaran, S. Hari, and M. Amirthalingam, Wire Arc Additive Manufacturing of Functionally Graded Material for Marine Risers, *Mater. Sci. Eng., A*, 2020, **792**, p 139530. <https://doi.org/10.1016/j.msea.2020.139530>
3. Y. Ayan, and N. Kahraman, Fabrication and Characterization of Functionally Graded Material (FGM) Structure Containing Two Dissimilar Steels (ER70S-6 and 308LSi) by Wire Arc Additive Manufacturing (WAAM), *Mater. Today Comm.*, 2022, **33**, p 104457–104457. <https://doi.org/10.1016/j.matcomm.2022.104457>
4. T.A. Rodrigues, N. Bairrão, F.W.C. Farias, A. Shamsolhodaei, J. Shen, N. Zhou, E. Maawad, N. Schell, T.G. Santos, and J.P. Oliveira, Steel-Copper Functionally Graded Material Produced by Twin-Wire and Arc Additive Manufacturing (T-WAAM), *Mater. Des.*, 2022, **213**, 110270. <https://doi.org/10.1016/j.matdes.2021.110270>
5. Y. Tian, J. Shen, S. Hu, Z. Wang, and J. Gou, Microstructure and Mechanical Properties of Wire and Arc Additive Manufactured Ti-6Al-4V and AlSi5 Dissimilar Alloys Using Cold Metal Transfer Welding, *J. Manuf. Processes.*, 2019, **46**, p 337–344. <https://doi.org/10.1016/j.jmapro.2019.09.006>
6. V. Hosseini, L. Karlsson, C. Örnek, P. Reccagni, S. Wessman, and D. Engelberg, Microstructure and Functionality of a Uniquely Graded Super Duplex Stainless Steel Designed by a Novel Arc Heat Treatment Method, *Mater. Charact.*, 2018, **139**, p 390–400. <https://doi.org/10.1016/j.matchar.2018.03.024>
7. J. Rodriguez, K. Hoefler, A. Haelsig, and P. Mayr, Functionally Graded SS 316L to Ni-Based Structures Produced by 3D Plasma Metal Deposition, *Metals*, 2019, **9**(6), p 620. <https://doi.org/10.3390/met9060620>
8. T.S. Senthil, S.R. Babu, and M. Puviyarasan, Mechanical, Microstructural and Fracture Studies on Inconel 825–SS316L Functionally Graded Wall Fabricated by Wire Arc Additive Manufacturing, *Sc. Rep.*, 2023 <https://doi.org/10.1038/s41598-023-32124-3>
9. P. Kumar, S.K. Sharma, and R.K.R. Singh, Recent Trends and Future Outlooks in Manufacturing Methods and Applications of FGM: A Comprehensive Review, *Mater. Manuf. Processes.*, 2022 <https://doi.org/10.1080/10426914.2022.2075892>
10. M. Lervåg, C. Sørensen, A. Robertstad, B.M. Brønstad, B. Nyhus, M. Eriksson, R. Aune, X. Ren, O.M. Akselsen, and I. Bunaziv, Additive Manufacturing with Superduplex Stainless Steel Wire by CMT Process, *Metals*, 2020, **10**(2), p 272. <https://doi.org/10.3390/met10020272>
11. A. Sales, A. Kotousov, and L. Yin, Design against Fatigue of Super Duplex Stainless Steel Structures Fabricated by Wire Arc Additive Manufacturing Process, *Metals*, 2021, **11**(12), p 1965. <https://doi.org/10.3390/met11121965>
12. D. Zhang, A. Liu, B. Yin, and P. Wen, Additive Manufacturing of Duplex Stainless Steels—a Critical Review, *J. Manuf. Process.*, 2022, **73**, p 496–517. <https://doi.org/10.1016/j.jmapro.2021.11.036>
13. A.R. Kannan, N.S. Shanmugam, K.D. Ramkumar, and V. Rajkumar, Studies on Super Duplex Stainless Steel Manufactured by Wire Arc Additive Manufacturing, *Trans. Indian Inst. Metals*, 2021 <https://doi.org/10.1007/s12666-021-02257-y>
14. W. Yangfan, C. Xizhang, and S. Chuanchu, Microstructure and mechanical properties of Inconel 625 fabricated by wire-arc additive manufacturing, *Surf. Coat. Technol.*, 2019, **374**, p 116–123
15. Y. Tian, J. Shen, S. Hu, Z. Wang, and J. Gou, Microstructure and Mechanical Properties of Wire and Arc Additive Manufactured Ti-6Al-4V and AlSi5 Dissimilar Alloys Using Cold Metal Transfer Welding, *J. Manuf. Process.*, 2019, **46**, p 337–344. <https://doi.org/10.1016/j.jmapro.2019.09.006>
16. W. Wu, W. Xu, J. Xue, and P. Yao, Effect of Cooling and CMT Mode Process on Additive Manufacturing, *Mater. Manuf. Process.*, 2022, **37**(11), p 1298–1309. <https://doi.org/10.1080/10426914.2021.2006221>
17. G.P. Rajeev, M. Kamaraj, and S.R. Bakshi, Effect of Correction Parameters on Deposition Characteristics in Cold Metal Transfer Welding, *Mater. Manuf. Processes.*, 2019, **34**(11), p 1205–1216. <https://doi.org/10.1080/10426914.2019.1628260>
18. T. Kumar, D.V. Kiran, N. Arora, and P.S. Kumar, Study of Steel-Aluminium Joining under the Influence of Current Waveforms Using Advanced CMT Process Variants, *Mater. Manuf. Process.*, 2022, **37**(13), p 1578–1595
19. S.H. Lee, CMT-Based Wire Arc Additive Manufacturing Using 316L Stainless Steel: Effect of Heat Accumulation on the Multi-Layer Deposits, *Metals*, 2020, **10**(2), p 278. <https://doi.org/10.3390/met10020278>
20. Z. Wang, S. Zimmer-Chevret, F. Leonard, C. Bourlet, and G. Abba, In Situ Monitoring of Internal Defects by a Laser Sensor for CMT Based Wire-Arc Additive Manufacturing Parts, *Defect Diffus. Forum*, 2022, **417**, p 67–72. <https://doi.org/10.4028/p-842jz0>
21. S. Zhou, H. Xie, J. Ni, G. Yang, L. Qin, and X. Guo, Metal Transfer Behavior during CMT-Based Wire Arc Additive Manufacturing of Ti-6Al-4V Alloy, *J. Manuf. Process.*, 2022, **82**, p 159–173. <https://doi.org/10.1016/j.jmapro.2022.07.063>
22. T. Tankova, D. Andrade, R. Branco, C. Zhu, D. Rodrigues, and L. Simões da Silva, Characterization of Robotized CMT-WAAM Carbon Steel, *J. Constr. Steel Res.*, 2022, **199**, p 107624. <https://doi.org/10.1016/j.jcsr.2022.107624>
23. X. Bi, R. Li, Z. Hu, J. Gu, and C. Jiao, Microstructure and Texture of 2205 Duplex Stainless Steel Additive Parts Fabricated by the Cold Metal Transfer (CMT) Wire and Arc Additive Manufacturing (WAAM), *Metals*, 2022, **12**(10), p 1655. <https://doi.org/10.3390/met12101655>
24. Y. Koli, S. Arora, S. Ahmad et al., Investigations and Multi-response Optimization of Wire Arc Additive Manufacturing Cold Metal Transfer Process Parameters for Fabrication of SS308L Samples, *J. Mater. Eng. Perform.*, 2023, **32**, p 2463–2475. <https://doi.org/10.1007/s11665-022-07282-6>
25. D. Yang, H. Fang, Y. Peng et al., Investigation of Spatters in Cold Metal Transfer + Pulse-Based Wire and Arc Additive Manufacturing of High Nitrogen Austenitic Stainless Steel, *J. Mater. Eng. Perform.*, 2021, **30**, p 6881–6894. <https://doi.org/10.1007/s11665-021-06048-w>
26. A.A. Ferreira, O. Emadinia, J.M. Cruz, A.R. Reis, and M.F. Vieira, Inconel 625/AISI 413 Stainless Steel Functionally Graded Material Produced by Direct Laser Deposition, *Materials*, 2021, **14**, p 5595. <https://doi.org/10.3390/ma14195595>
27. Bo. Chen, Su. Yi, Z. Xie, C. Tan, and J. Feng, Development and Characterization of 316L/Inconel625 Functionally Graded Material Fabricated by Laser Direct Metal Deposition, *Opt. Laser Tech.*, 2020, **123**, p 105916. <https://doi.org/10.1016/j.optlastec.2019.105916>
28. P. Li, Y. Gong, Xu. Yunchao, Y. Qi, Y. Sun, and H. Zhang, Inconel-Steel Functionally Bimetal Materials by Hybrid Directed Energy Deposition and Thermal Milling: Microstructure and Mechanical Properties, *Arch. Civ. Mech. Eng.*, 2019, **19**(3), p 820–831. <https://doi.org/10.1016/j.acme.2019.03.002>

29. D.R. Feenstra, A. Molotnikov, and N. Birbilis, Effect of Energy Density on the Interface Evolution of Stainless Steel 316L Deposited Upon INC 625 Via Directed Energy Deposition, *J. Mater. Sci.*, 2020, **55**, p 13314–13328. <https://doi.org/10.1007/s10853-020-04913-y>
30. R. Zhang, N. Bian, Lu. Hongbing, Y. Li, Yi. Tian, and W. Li, Molten Pool Swing in Printing the Steel/Inconel Functionally Gradient Material with Laser-Based Directed Energy Deposition, *Manuf. Lett.*, 2022, **32**, p 44–48. <https://doi.org/10.1016/j.mfglet.2022.03.002>
31. V.A. Popovich, E.V. Borisov, A.A. Popovich, VSh. Sufiarov, D.V. Masaylo, and L. Alzina, Functionally Graded Inconel 718 Processed by Additive Manufacturing: Crystallographic Texture, Anisotropy of Microstructure and Mechanical Properties, *Mat. Des.*, 2017, **114**, p 441–449. <https://doi.org/10.1016/j.matdes.2016.10.075>
32. A. Rajesh Kannan, S. Mohan Kumar, R. Pramod, N. Siva Shanmugam, M. Vishnukumar, and S. Naveenkumar, Microstructural Characterization and Mechanical Integrity of Stainless Steel 316L Clad Layers Deposited Via Wire Arc Additive Manufacturing for Nuclear Applications, *Mater. Sci. Eng. Tech*, 2021 <https://doi.org/10.1002/mawe.202000242>
33. S. Mohan Kumar, A. Rajesh Kannan, N. Pravin Kumar et al., Microstructural Features and Mechanical Integrity of Wire Arc Additive Manufactured SS321/Inconel 625 Functionally Gradient Material, *J. Mater. Eng. Perform.*, 2021, **30**, p 5692–5703. <https://doi.org/10.1007/s11665-021-05617-3>
34. A. Khajuria, R. Kumar, and R. Bedi, Effect of Boron Addition on Creep Strain During Impression Creep of P91 Steel, *J. Mater. Eng. Perform.*, 2019, **28**, p 4128–4142. <https://doi.org/10.1007/s11665-019-04167-z>
35. D.D.S. Silva, T.A. Simões, D.A. Macedo, A.H.S. Bueno, S.M. Torres, and R.M. Gomes, Microstructural Influence of Sigma Phase on Pitting Corrosion Behavior of Duplex Stainless Steel/NaCl Electrolyte Couple, *Mater. Chem. Phys.*, 2021 <https://doi.org/10.1016/j.matchemphys.2020.124056>
36. W. Yongqiang, S. Hao, L. Na, X. Yanhao, and J. Hemin, Effect of Sigma Phase Precipitation on the Pitting Corrosion Mechanism of Duplex Stainless Steels, *Int. J. Electrochem. Sci.*, 2018, **13**(10), p 9868–9887. <https://doi.org/10.20964/2018.10.38>
37. V.A. Hosseini, L. Karlsson, S. Wessman, and N. Fuertes, Effect of Sigma Phase Morphology on the Degradation of Properties in a Super Duplex Stainless Steel, *Materials (Basel)*, 2018, **11**(6), p 933. <https://doi.org/10.3390/ma11060933>
38. G. Lothongkum and S. Chaikittisilp, Lothongkum AW XPS investigation of surface films on high Cr-Ni ferritic and austenitic stainless steels, *Appl. Surf. Sci.*, 2003, **218**, p 203–210
39. C.M. Abreu, M.J. Cristobal, and R. Losada, The effect of Ni in the electrochemical properties of oxide layers grown on stainless steels, *Electrochim. Acta*, 2006, **51**, p 2991–3000

Publisher's Note Springer Nature remains neutral with regard to jurisdictional claims in published maps and institutional affiliations.

Springer Nature or its licensor (e.g. a society or other partner) holds exclusive rights to this article under a publishing agreement with the author(s) or other rightsholder(s); author self-archiving of the accepted manuscript version of this article is solely governed by the terms of such publishing agreement and applicable law.